



# Numerical Simulation on Refractory Wear and Inclusion Formation in Continuous Casting Tundish

QIANG WANG, CHONG TAN, AO HUANG, WEN YAN, HUAZHI GU, ZHU HE, and GUANGQIANG LI

The formation and removal of exogenous inclusions in a real-size two-strand tundish is simulated by the proposed unsteady 3D comprehensive numerical model of the respective fluid-structure interaction, which takes into account the impacting and washing effects on the refractory wear. A large eddy simulation is employed to describe the molten steel vortex flow. Thus, the thermal profiles of the molten steel and refractory lining are constructed. One-way coupled unsteady Euler-Lagrange approach is adopted to estimate the detachment and motion of the exogenous inclusion. The inclusion's Reynolds number is utilized for evaluating the inclusion separation at the refractory lining after formation and at the upper surface of the molten steel. At a 1.2 m/min casting speed, 49 and 38 pct of exogenous inclusions are created at the turbulent inhibitor inner bottom and long nozzle inner wall, respectively. In contrast, only 13 pct of new inclusions are produced at all other inner walls. About 80 pct of newly generated inclusions are then trapped by free surfaces, 78 pct of which are removed at the first free surface. The initial diameter of exogenous inclusions ranges from 13 to 48  $\mu\text{m}$ . The removal ratio of exogenous inclusions in the tundish first grows from 61 to 80 pct, with the casting speed rising from 1.0 to 1.2 m/min and then drops to 63 pct after the further casting speed rise to 1.4 m/min.

<https://doi.org/10.1007/s11663-021-02097-7>

© The Minerals, Metals & Materials Society and ASM International 2021

## I. INTRODUCTION

HIGH-QUALITY steels have excellent mechanical properties due to the mandatory absence of macroscopic inclusions and a very low number of microscopic ones (smaller than 10  $\mu\text{m}$ ).<sup>[1–3]</sup> According to their formation sources, inclusions can be classified into two types. The first-type ones are named indigenous inclusions that stem from deoxidation products, such as  $\text{Al}_2\text{O}_3$  and  $\text{SiO}_2$ . They are usually small (*i.e.*, micro inclusions) and can be easily removed using various refining measures. The second-type ones are referred to as exogenous inclusions, mainly from refractory wear and slag entrapment. The equivalent diameters of exogenous inclusions are in the range of tens to hundreds of

micrometers (*i.e.*, macro inclusions), which deteriorate the steel quality.<sup>[4–7]</sup> Since the molten steel mostly contacts with the refractory lining in the continuous casting process, exogenous inclusions' formation is fraught with chance and hard to eliminate.

In the continuous casting process, tundish (*i.e.*, the last refractory container located between the ladle and mold) is designed to receive the molten steel poured from the ladle and distribute the molten steel to the different continuous casting machine strands at a near-constant rate. Because of the large volume and stable dynamic conditions, the tundish is believed to be an appropriate place for cleaning the molten steel.<sup>[8,9]</sup> Therefore, various flow control devices, such as weir, dam, and turbulence inhibitors, have been adopted, to optimize the flow pattern and promote the inclusion removal. Recently, the main function of the tundish was changed from a reservoir to a refining vessel. However, the impact flow from the ladle, large internal surface area of the tundish, and increasing number of flow control devices provide more opportunities for the accidental formation of exogenous inclusions inside the tundish, as shown in Figure 1.<sup>[10]</sup>

QIANG WANG, CHONG TAN, AO HUANG, WEN YAN, HUAZHI GU, ZHU HE, and GUANGQIANG LI are with the The State Key Laboratory of Refractories and Metallurgy, Wuhan University of Science and Technology, Wuhan 430081, Hubei, China and also with the Key Laboratory for Ferrous Metallurgy and Resources Utilization of Ministry of Education, Wuhan University of Science and Technology, Wuhan 430081, Hubei, China. Corresponding author: [liguangqiang@wust.edu.cn](mailto:liguangqiang@wust.edu.cn)

Manuscript submitted October 10, 2020; accepted January 27, 2021.

Article published online March 2, 2021.

To further improve the molten steel's cleanliness, it is expedient to gain a deeper insight into the refractory wear and inclusion formation in the tundish.<sup>[11–13]</sup> An industrial experiment on a real tundish is the most intuitive and straightforward method for studying the refractory wear, as illustrated in Figure 2.

However, the measurement limitations and harsh environment in the above test scheme deteriorate the accuracy and scope of experimental results. In particular, the formation of exogenous inclusions cannot be observed, and it is difficult to distinguish the indigenous and exogenous inclusions in steel samples.

The water model experiment has been widely adopted to visualize the flow pattern and inclusion motion in tundish with different flow control devices.<sup>[14–17]</sup> In the experiment, salt solutions, such as KCl and NaCl, are commonly used as tracers to measure the residence time distribution (RTD) curve of water in the tundish physical model. Black ink and polyethylene particle are usually applied to represent the water flow pattern and inclusion motion trajectory. The particle image velocimetry measurement technique is then utilized to estimate the velocity field, and a high-speed camera is employed to capture the polyethylene particle position at different moments. The refractory wear behavior can

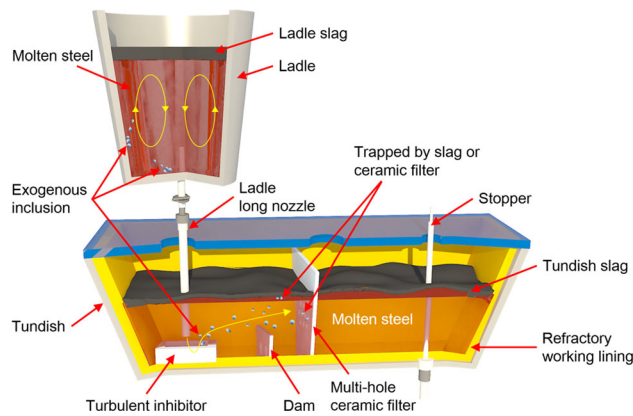


Fig. 1—Schematic of fluid flow and inclusion motion in a single strand tundish.



Fig. 2—Photo of the tundish refractory lining after one casting period.

also be simulated using the water model with a boric acid tablet on the wall.<sup>[18]</sup> As the boric acid is soluble in water, it would be gradually removed when the water passes through the tablet surface. The removal rate can be related to the wall shear stress, which is predicted by numerical simulations.<sup>[19]</sup> However, the water model fails to reflect the inclusion formation process induced by the refractory wear.

Alternatively, the computational fluid dynamics (CFD) approach has become a powerful tool for analyzing the flow-induced wall shear stress and tracking the inclusion motion in tundishes.<sup>[20]</sup> Since the flow-induced wall shear stresses would significantly reduce the service life of the tundish refractory lining, especially in the high-velocity region near the inlet stream, multiple numerical models have been proposed to optimize the tundish shape and furniture design using the wall shear stress as a function of the near-wall velocity gradient.<sup>[21]</sup> Furthermore, the refractory wear was found to be affected by the combined influence of the wall shear stresses and the molten steel total pressure.<sup>[22,23]</sup> The refractory deformation and erosion behavior strongly depend on the flow regime nature and fluid-structure interaction, as indicated in Figure 3.<sup>[24,25]</sup> The understanding of fluid-structure interaction between molten steel and the refractory lining, however, is limited by far.

The well-known Euler–Lagrangian method has been commonly employed to describe the motion, collision, and aggregation of inclusions.<sup>[26,27]</sup> It allows one to consider such factors as gravity, buoyancy, drag, lift, virtual mass, pressure gradient forces, and turbulent fluctuation of the inclusions. Comprehensive analysis of the inclusion parameters, such as its position, diameter, and velocity during entire motion process, can be adequately performed. Besides, various detachment criteria have been introduced into the numerical model to represent the adherence between the inclusion and the refractory wall.<sup>[28–30]</sup> When the inclusion migrates and gets into contact with the refractory wall, the inclusion would adhere to the wall or rebound into the molten steel with a certain momentum loss, which can be appropriately described *via* the elastic collision theory.

As discussed above, the refractory wear is created by the wall shear stresses and total pressure of the molten steel. The resultant inclusion formation in the tundish and possible improvement of the molten steel cleanliness require further investigation. This encouraged the authors to establish a transient 3D integrated numerical model to figure out the fluid-structure interaction and the resultant inclusion formation in a two-strand tundish. Since a small-scale vortex near the tundish internal wall greatly affects the inclusion formation and detachment, a large eddy simulation was employed to describe the molten steel turbulent flow. The thermal profile of the molten steel and refractory lining was also constructed. Given the inclusion concentration in the molten steel is very small, the inclusion movement's effect on the molten steel flow is negligible. One-way coupled unsteady Euler–Lagrange approach was adopted to estimate the motion path of the inclusion. The inclusion's Reynolds number was utilized to

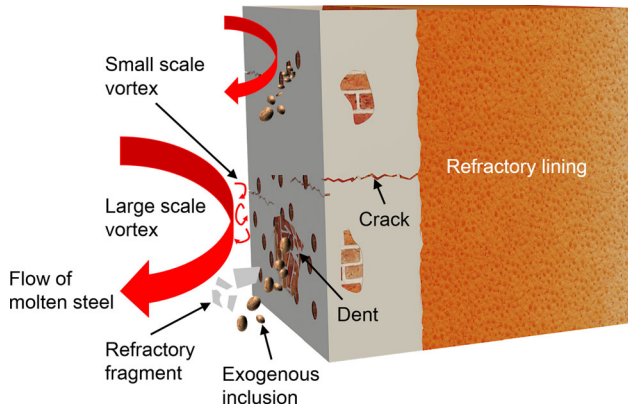


Fig. 3—Fluid-structure interaction between molten steel, refractory, and formed exogenous inclusion.

evaluate the inclusion separation at the refractory lining after formation and at the top surface of the molten steel, instead of the ideal absorption condition used in previous works.<sup>[31]</sup> The casting speed effect on the inclusion removal was analyzed using the proposed model.

## II. MODEL DESCRIPTION

### A. Assumptions

Given the complex fluid–solid interaction and transport phenomena involved in the tundish, the following assumptions were made to simplify the model:

- Only a half the tundish was modeled because of its geometrical symmetry.
- The solid part included the long nozzle, turbulent inhibitor, weir, dam, and refractory lining, while the fluid part only involved the molten steel, *i.e.*, the molten slag and air were neglected. Due to the absence of molten slag, the chemical corrosion was ignored. Besides, the wall shear stress caused by the molten steel/molten slag two phase flow at the refractory lining that near the slag/steel interface is different from that caused only by the molten steel.
- The molten steel was treated as an incompressible Newtonian fluid. The density, thermal conductivity, and viscosity of the molten steel were a function of the temperature. Besides, the Young modulus of the refractory material was temperature dependent.<sup>[32]</sup> The other properties were assumed to be constant.
- No inclusion would come into the tundish with the molten steel from the ladle. The inclusion was supposed to be generated at the refractory tundish inner wall and treated as an inert non-spherical solid body.<sup>[8]</sup>
- The coefficient of the interfacial tension coefficient between the molten steel and the inclusion was kept constant.
- Chemical reactions in the tundish were neglected, *i.e.*, the refractory chemical corrosion was ignored.

### B. Fluid Flow and Heat Transfer

The wall shear stresses and dynamic pressure on the wall were reported to be closely associated with the near-wall vortices.<sup>[33,34]</sup> To better describe the turbulent fluctuation, the large eddy simulation (LES) model was employed to analyze the vortex structure inside the tundish.<sup>[35–37]</sup> The continuity and time-dependent Navier-Stokes equations were invoked to describe the molten steel turbulent flow in the tundish:

$$\frac{\partial \rho_m}{\partial t} + \nabla \cdot (\rho_m \vec{v}) = 0, \quad [1]$$

$$\begin{aligned} \frac{\partial(\rho_m \vec{v})}{\partial t} + \rho_m(\vec{v} \cdot \nabla)\vec{v} = & -\nabla p + \nabla \\ & \cdot [(\mu + \mu_{sgs})(\nabla \vec{v} + \nabla \vec{v}^T)] + \vec{F}_t, \end{aligned} \quad [2]$$

where  $t$  is time,  $\vec{v}$  is velocity,  $p$  is pressure,  $\rho_m$  is the molten steel density, and  $\mu$  and  $\mu_{sgs}$  are the molten steel dynamic viscosity and eddy viscosity that represents the sub-grid scale stress, respectively, and the eddy viscosity is derived *via* the coherent structure wall-adapting local eddy viscosity (WALE) model of sub-grid scales.<sup>[38]</sup> Besides,  $\vec{F}_t$  is the thermal buoyancy force determined by the Boussinesq approximation.

The energy conservation equation was established in the fluid and solid regions for obtaining the temperature profile:

$$\text{In fluid region : } \frac{\partial(\rho_m h)}{\partial t} + \nabla \cdot (\rho_m \vec{v} h) = \nabla \cdot (k_{\text{eff}} \nabla T), \quad [3]$$

$$\text{In solid region : } \frac{\partial T}{\partial t} = \nabla \cdot (k_T \nabla T), \quad [4]$$

where  $h$  is enthalpy,  $T$  is temperature, and  $k_{\text{eff}}$  is the effective thermal conductivity of the molten steel that relating to the turbulent level, while  $k_T$  is the thermal conductivity of the refractory.

### C. Structural Model

Due to the action of continuous forces induced by the molten steel flow, the refractory displacement occurs, which can be assessed using the following momentum equation:<sup>[39,40]</sup>

$$\begin{aligned} -\rho_r \underline{a} + \frac{E}{1+v} \nabla \cdot \left[ \frac{v}{1-2v} \text{tr}(\underline{\nabla} \underline{u}) \underline{I} + \frac{1}{2} (\underline{\nabla} \underline{u} + (\underline{\nabla} \underline{u})^T) \right] \\ = 0, \end{aligned} \quad [5]$$

where  $\rho_r$  is the refractory density,  $\underline{a}$  is acceleration,  $\underline{I}$  is unit tensor,  $E$  is the Young modulus,  $v$  is Poisson's ratio, and  $\underline{u}$  is the displacement vector. The resulting stress  $\underline{\sigma}$  is derived by the constitutive equation as in:<sup>[41,42]</sup>

$$\underline{\underline{\sigma}} = \frac{E}{1+\nu} \left( \frac{\nu}{1-2\nu} \text{tr}(\underline{\underline{\varepsilon}}) \underline{\underline{I}} + \underline{\underline{\varepsilon}} \right), \quad [6]$$

$$\underline{\underline{\varepsilon}} = \frac{1}{2} \left[ \underline{\underline{\nabla u}} + \left( \underline{\underline{\nabla u}} \right)^T \right], \quad [7]$$

where  $\underline{\underline{\varepsilon}}$  was the deformation tensor.

The von Mises stress, invoked in the von Mises criterion, anticipating the occurrence of yielding of the refractory, can be evaluated as:<sup>[43,44]</sup>

$$\sigma_v = \left( \frac{1}{2} \left[ (\sigma_{xx} - \sigma_{yy})^2 + (\sigma_{yy} - \sigma_{zz})^2 + (\sigma_{zz} - \sigma_{xx})^2 + 6(\sigma_{xy}^2 + \sigma_{yz}^2 + \sigma_{xz}^2) \right] \right)^{\frac{1}{2}}. \quad [8]$$

Since the above equation is algebraic, the von Mises stress can be estimated from the previously calculated stress components.

#### D. Refractory Physical Wear

As mentioned above, the refractory physical wear is determined by the combined effect of the wall shear stress and total pressure. According to the rotating disk theory, the wall shear stress-induced wear rate  $w_{wss}$  can be estimated *via* the following equation:<sup>[45-47]</sup>

$$w_{wss} = k_{wss} \left( \frac{\tau}{\tau_{ref}} \right)^{1/3} \quad [9]$$

where  $\tau$  indicates the wall shear stress at the interface between the molten steel and the refractory in the tundish,  $\tau_{ref}$  is reference wall shear stress, and  $k_{wss}$  is the refractory dissolution rate that can be derived from the molten steel temperature  $T$  as follows:<sup>[48]</sup>

$$k_{wss} = 0.01 \cdot \exp \left[ 2.8956 - \left( \frac{11,344}{T} \right) \right]. \quad [10]$$

The wear rate  $w_{tp}$  caused by the total pressure has the following form:<sup>[49,50]</sup>

$$w_{tp} = g(\theta) W_{90}, \quad [11]$$

$$g(\theta) = (\sin \theta)^{n1} [1 + Hv(1 - \sin \theta)]^{n2}, \quad [12]$$

$$W_{90} = k_{tp} (Hv)^{-0.12} \left( \frac{P_t}{P_{tref}} \right)^{k1}, \quad [13]$$

$$\begin{aligned} n1 &= 0.71(Hv)^{0.14}, \quad n2 = 2.4(Hv)^{-0.94}, \\ k1 &= 2.3(Hv)^{0.038}, \end{aligned} \quad [14]$$

where  $\theta$  is the impact angle of the molten steel with respect to the refractory wall,  $Hv$  is the Vickers number (in GPa) of the refractory material,  $k_{tp}$  is the empirical constant, while  $P_t$  and  $P_{tref}$  are the molten steel total pressure and total reference pressure, respectively.

Since it is difficult to find a reasonable and accurate numerical model for quantifying the interaction between the two wear rates induced by the wall shear stress and total pressure, the final overall wear rate was assumed to be their superposition (sum). It should be noted that the final overall wear rate may have non-additive pattern, which would require further refinement of the above calculation approach. The mass flux of the newly generated inclusion at the refractory wall  $\dot{m}_p$  can be determined *via* the final overall wear rate as:<sup>[51-54]</sup>

$$\dot{m}_p = \rho_r A (w_{wss} + w_{tp}), \quad [15]$$

where  $A$  is the refractory wear area. The initial diameter of the newly generated inclusion is assumed to be proportional to the final overall wear rate:

$$d_p = d_{pref} \frac{w_{wss} + w_{tp}}{w_{ref}} \quad [16]$$

where  $d_{pref}$  and  $w_{ref}$  are the reference inclusion diameter and overall wear rate, respectively. The above equation is the empirical formula of the initial diameter of the newly generated inclusion caused by the refractory wear, based on our refractory/steel high-temperature experiments.

#### E. Inclusion Movement

In the present work, the one-way coupled unsteady Euler-Lagrange particle-tracking method was utilized to describe the inclusion trajectory after its formation at the refractory wall.<sup>[55]</sup> A transport equation was established for each inclusion, which considered contributions from seven different forces as indicated in Figure 4.<sup>[56]</sup>

$$\rho_p \frac{\pi}{6} d_p^3 \frac{d\vec{v}_p}{dt} = \vec{F}_g + \vec{F}_b + \vec{F}_d + \vec{F}_v + \vec{F}_l + \vec{F}_p \quad [17]$$

where  $\rho_p$ ,  $d_p$  and  $\vec{v}_p$  are the inclusion density, equivalent diameter, and velocity, respectively. The six terms in the above equation's right-hand side are gravity, buoyancy, drag, virtual mass, lift, and pressure gradient forces, respectively.

The random walk model was used for counting the chaotic effect of the turbulence.<sup>[57,58]</sup> The instantaneous velocity of the inclusion is the sum of mean velocity,  $\bar{v}_p$ , and random velocity,  $v'_p$ , which is proportional to the local turbulent kinetic energy of the molten steel  $k_m$ :

$$\vec{v}_p = \bar{v}_p + v'_p, \quad v'_p = \xi \sqrt{v_p'^2} = \xi \sqrt{\frac{2k_m}{3}} \quad [18]$$

where  $\xi$  is a Gaussian-distributed random number, with a zero mean value and the standard deviation of 1, that varies at each time step.

The stochastic collision model was invoked to cooperate with the one-way unsteady Euler-Lagrange particle-tracking approach and consider the inclusion's collision and aggregation.<sup>[59]</sup> The O'Rourke algorithm



was used to calculate the collision probability, while a random function determined the coalescence behavior.<sup>[60,61]</sup>

### F. Boundary Conditions

The physical structure of the tundish in the present work, as shown in Figure 5, followed a real plant-scale operating two-strand tundish, and typical plant operating conditions were employed as boundary conditions.

A mass flow rate, equal to half of the real mass flow rate, was imposed at the inlet with a constant turbulent kinetic energy and dissipation rate. The outlet was assumed to have the outflow boundary condition. A zero shear stress boundary condition was satisfied at the free surface of the molten steel. Additionally, a reference pressure at the free surface was set to a constant value, which equaled the atmospheric pressure.

As for the temperature profile, equivalent heat transfer coefficients with the values of 8.5, 15, and 15 W/(m<sup>2</sup> K) were, respectively, applied to the bottom, longitudinal, and transverse side outer walls of the solid refractory lining for illustrating the heat loss of the molten steel.<sup>[62,63]</sup> A thermally coupled boundary condition was set at the fluid/solid interfaces to account for the heat transfer fluid and solid regions. An equivalent emissivity and convection heat transfer coefficient with the values of 0.8 and 35 W/(m<sup>2</sup> K) were adopted to assess the heat dissipation through the molten steel's free surface.<sup>[64,65]</sup> The incoming molten steel temperature from the long nozzle was constant and equaled 1836 K (1563 °C).

Insofar as this study is focused on the refractory wear effect on the inclusion formation, it is reasonable to assume that no inclusion would enter the domain with the molten steel *via* the long nozzle. This assumption can imply differences in the experimental and simulated processes of the inclusion removal. However, it is difficult to distinguish the indigenous and exogenous inclusions, and the appearance of the indigenous inclusion would affect the motion of the exogenous one.<sup>[66–68]</sup> Therefore, the above assumption is considered instrumental in the in-depth analysis of the exogenous inclusion formation. The inclusion density was determined based on alumina, but considering that the actual inclusion is a mixture, a smaller inclusion density was therefore used in the present work.<sup>[67,69,70]</sup> Besides, the inclusion would be trapped at the molten steel's free surface if its Reynolds number is less than the threshold value. Otherwise, it would be rebounded with a certain amount of momentum loss, proportional to the inclusion's Reynolds number. The critical inclusion Reynolds number at the free surface was set as 3.5, and the inclusion equivalent diameter was adopted to be the characteristic length. A certain amount of momentum would be lost when the inclusion impacts solid walls.<sup>[71,72]</sup> The detailed physical properties and operating conditions are listed in Table I.

## III. SOLUTION PROCEDURE

The ANSYS Fluent 19.1 general purpose commercial software, based on the finite volume method, was employed in the numerical simulations. The governing equations for the fluid flow, heat transfer, inclusion formation and motion in the fluid region, and the solid region's temperature profile were integrated over each control volume and simultaneously solved using an iterative procedure. The development of the inclusion formation and entrapment model was accomplished by User Defined Function (UDF) feature in ANSYS Fluent. The PISO scheme was utilized for the pressure-velocity coupling, and the second-order upwind scheme was adopted for discretizing the pressure,

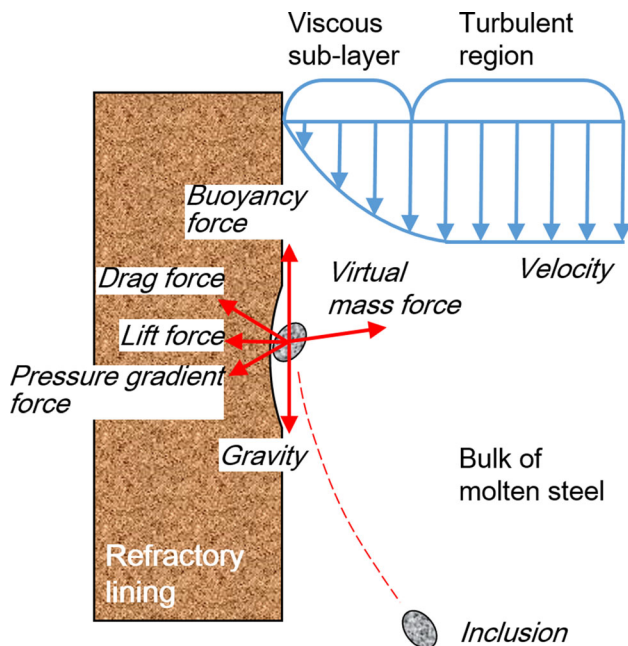


Fig. 4—Schematic of the inclusion motion near refractory wall after formation.

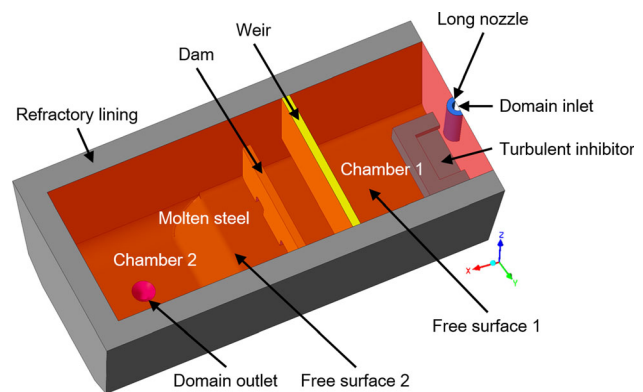


Fig. 5—Computational domain and boundaries.

**Table I. Physical Properties and Operating Conditions**

Parameter	Value
<i>Physical properties of molten steel</i>	
Density (kg/m <sup>3</sup> )	6992
Dynamic viscosity (Pa·s)	$1 \times 10^{-3} \times 10^{(2694.95/T - 0.7209)}$
Thermal conductivity (W/m·K)	$33.3 + 0.0215 \times (T - 1818)$
Specific heat (J/kg·K)	825
Thermal coefficient of cubical expansion (K <sup>-1</sup> )	$1.27 \times 10^{-4}$
<i>Physical properties of inclusion</i>	
Density (kg/m <sup>3</sup> )	3500
Coefficient of interfacial tension between inclusion and molten steel (N/m)	1.254
<i>Operating conditions</i>	
Mass flow rate of molten steel (kg/s)	130
Temperature of incoming molten steel (K)	1836
Volume of molten steel in tundish (m <sup>3</sup> )	10.27

momentum, energy, and structure equations for higher accuracy. Default values of the under-relaxation factors were used. The convergence criteria for the continuity, momentum, and structure equations were set at  $10^{-6}$ , while that for the energy equation was  $10^{-8}$ . Three sets of the structured meshes, with the respective mean sizes of 1, 3, and 5 mm, were first created. After a typical simulation, the velocity magnitude of some key points inside the tundish for the three types of the grids were examined. The average deviation of the velocity magnitude at all the points for the first and second meshes is about 4.65 pct, while it is approximately 8.36 pct between the second and the third meshes. Considering the high expensive of computation, we therefore used the second mesh for obtaining a reasonable balance between the computational cost and accuracy. The total number of grid elements was about three million. All simulation scenarios were conducted with a  $1 \times 10^{-4}$  s time step. A complete scenario needed approximately 400 CPU hours with 40 compute cores of 4.0 GHz.

#### IV. RESULTS AND DISCUSSION

##### A. Flow Pattern and Temperature Distribution

Figure 6 depicts the 3D flow streamlines in the tundish at 500 seconds. The common routine for the molten steel flow is as follows: ① the molten steel flows into the turbulent inhibitor from the long nozzle and moves upward due to the turbulent inhibitor’s restriction. The upper molten steel then moves downwards to the gap between the weir and the refractory bottom lining because of the obstruction of the weir, ② after leaving the first chamber, the molten steel moves upwards as a result of the dam’s blocking, while a small amount of molten steel directly flows to the second chamber along the refractory bottom lining through the dam hole, ③ after entering the larger second chamber, the molten steel continuously migrates upwards under the action of the inertia, then moves along the free surface toward the transverse sidewall, and finally falls

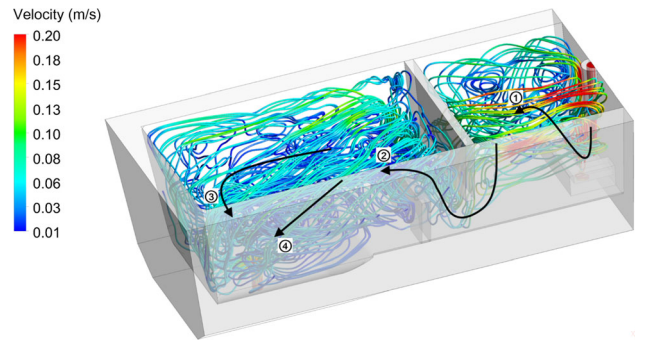


Fig. 6—Distribution of 3D flow streamlines in tundish at 500 s.

to the outlet, ④ a part of molten steel moves downwards to the bottom of the second chamber due to the buoyancy, thus creating a short-circuit flow.

Figure 7 illustrates the  $Q$ -criterion’s distribution iso-surface of 350, where the color indicates the magnitude of vorticity in the tundish at 500 seconds. The  $Q$ -criterion is directly derived based on the second invariant  $Q$  of the velocity gradient tensor as:<sup>[73–75]</sup>

$$Q = \frac{1}{2} \left( \|\Omega\|^2 - \|S\|^2 \right) \quad [19]$$

where  $\Omega$  is the antisymmetric part known as the vorticity tensor, and  $S$  is the symmetric part known as the rate of strain. According to the definition, the  $Q$ -criterion indicates the existence or absence of vortices in various flow structures. Numerous vortices are triggered inside the long nozzle, turbulent inhibitor, and first chamber. Furthermore, the magnitude of vorticity in the long nozzle and turbulent inhibitor is much higher. It can be inferred that the mixing of the molten steel in the first chamber is vigorous. Due to the weir and dam’s impeding and the refractory lining friction, the energy dissipation is enhanced, and these vortices gradually decay. The number of vortices in the second chamber obviously decreases.

Figure 8 shows the temperature distribution on the middle longitudinal section ( $Y = 0$  m) of the tundish at 500 seconds. The highest temperature is observed at the inlet, while the lowest temperature occurs at the second chamber's top left corner, due to higher heat loss. As the molten steel travels through the entire tundish, it loses a total of 16 K (16 °C) of superheat. Since the hotter molten steel heats the refractory lining's inner layer, the latter's temperature gradually increases. The average temperature of the refractory lining's outer layer is about 480 K (207 °C), which agrees well with the actual tundish measurements. The measurement data provided by plant were in the range of 473 K to 489 K (200 °C to 216 °C).

### B. Distribution of Wear Rate

Figure 9 depicts the distribution of wall shear stresses along the entire internal refractory wall and a close-up of the long nozzle inner wall and turbulent inhibitor inner bottom at 500 seconds. Higher wall shear stresses are observed at the turbulent inhibitor inner bottom and outlet wall, especially the long nozzle inner wall, due to a higher velocity and a confined space. Besides, the wall shear stress distribution is asymmetric at this moment, although the tundish structure is symmetric. As mentioned above, various-scale vortices would be triggered in the molten steel by the refractory wall effect. The generation and dissipation of these vortices then give rise to an asymmetrical variation in the transient flow structure, which is believed to be an intrinsic characteristic of the turbulent flow. The large eddy simulation is considered to be able to depict the asymmetrical flow behavior of molten steel. As can be observed, the wall

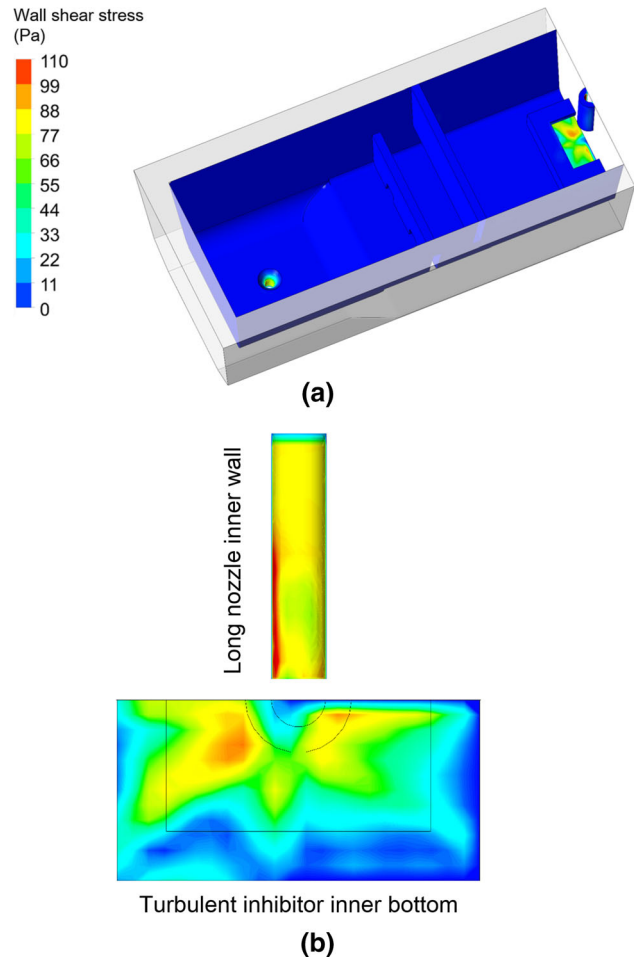


Fig. 9—Distribution of the wall shear stress on the entire internal refractory wall (a) and a close-up of the long nozzle inner wall and turbulent inhibitor inner bottom (b) at 500 s.

shear stress in the center of the turbulent inhibitor inner bottom just underneath the long nozzle is lower than that on the surrounding area. This is because the wall shear stress is determined by the velocity gradient that represents the washing effect of the molten steel on the refractory wall.

Figure 10 displays the wear rate distribution induced by the wall shear stress along the entire internal refractory wall at 500 seconds. According to Eq. [9], the wear rate is directly proportional to the wall shear stress; and as a result, its distribution pattern follows the wall shear stress map. The molten steel would seriously wash the inner refractory lining of the long nozzle, turbulent inhibitor, and outlet.

Besides the washing effect, the molten steel would also have an impacting effect on the refractory wall. The resultant wear rate is determined by the total pressure and flow angle, as mentioned above. As the long nozzle flow is not completely parallel to the vertical direction, the high-speed molten steel would impact the long nozzle inner wall, resulting in greater total pressure, as indicated in Figure 11. The molten steel then strikes against the turbulent inhibitor's inner bottom after flowing from the long nozzle. It can be seen that a higher

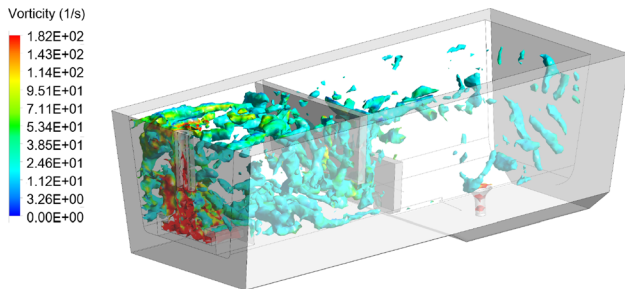


Fig. 7—Distribution of the  $Q$ -criterion iso-surface of 350, where the color indicates the magnitude of vorticity in the tundish at 500 s.

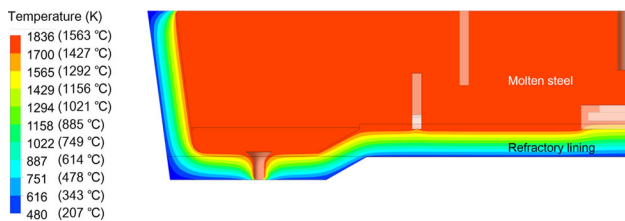


Fig. 8—Temperature distribution on the middle longitudinal section ( $Y = 0$  m) of tundish at 500 s.



total pressure is generated in the center of the turbulent inhibitor inner bottom below the long nozzle, where the wall shear stress is lower. Furthermore, the distribution of the total pressure is also asymmetrical at this moment.

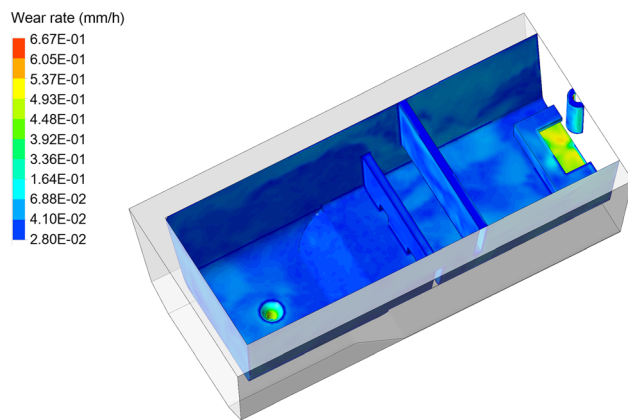


Fig. 10—Distribution of the wear rate caused by the wall shear stress on the entire internal refractory wall at 500 s.

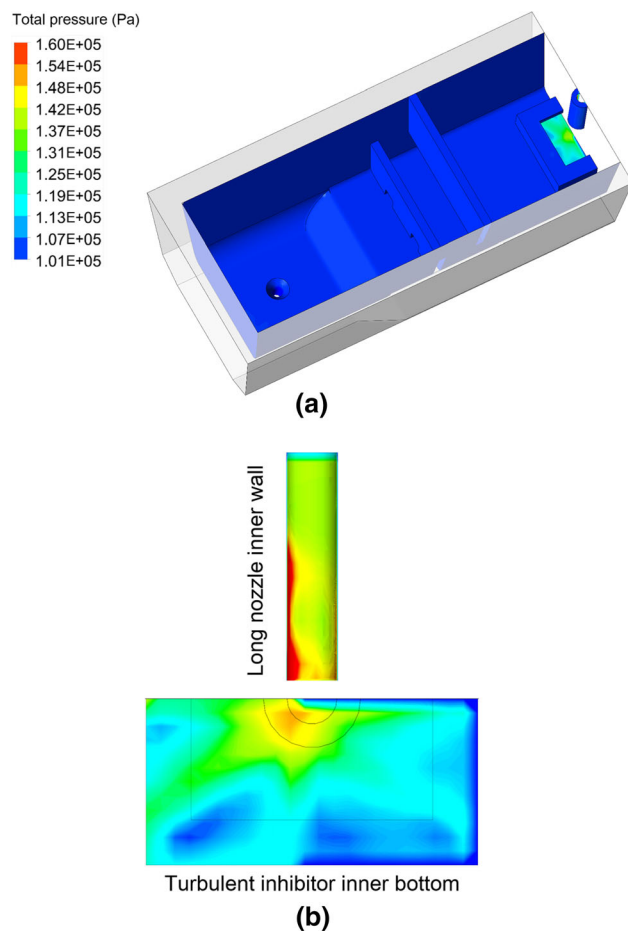


Fig. 11—Distribution of the total pressure on the entire internal refractory wall (a) and a close-up of the long nozzle inner wall and turbulent inhibitor inner bottom (b) at 500 s.

Figure 12 illustrates the wear rate profile induced by the total pressure. The most serious wear is observed at the long nozzle inner wall and turbulent inhibitor inner bottom, as expected. The inner refractory lining of the first chamber is also subjected to a certain extent of wear. However, the wear rate induced by the impacting effect is lower by one order of magnitude than that of the washing effect. It is mainly because the refractory resistance to pressurizing is more advantageous than that of the polishing (washing) effect.

Figure 13 depicts the distribution of the overall wear rate (derived as a sum of two wear rates mentioned above) on the entire internal refractory wall at 500 seconds. The overall wear rate distribution is similar to that caused by the wall shear stress. The most damaged areas are the long nozzle inner wall and turbulent inhibitor inner bottom. Due to the turbulent flow's unsteady characteristics, the wear rate distribution is non-uniform and time dependent, especially at the turbulent inhibitor inner bottom.

Figure 14 depicts the von Mises stress distribution along the entire internal refractory wall at 500 seconds. The von Mises stress is controlled by the fluid acceleration, according to Eq. [5] Higher von Mises stresses are observed at the walls of the long nozzle, turbulent inhibitor, weir, and dam, because this tundish configuration strongly affects flow characteristic of the molten steel. The highest von Mises stress is found at the long nozzle wall due to the rapid increase of the molten steel velocity magnitude. In contrast, the molten steel flow is dramatically hindered by the turbulent inhibitor, weir, and dam. Although the velocity magnitude change inside the turbulent inhibitor is more dramatic, the von Mises stresses at the weir and dam walls are higher than at the turbulent inhibitor bottom. This can be attributed to the refractory pressurizing resistance mentioned above.

Figure 15 displays the total refractory displacement at 500 seconds. The von Mises stress can be used as the distortion indicator of the refractory material: higher von Mises stresses correspond to larger total displacements. As expected, the refractory's largest deformation of 1.95 mm was observed at the lower part of the long nozzle, while those of other tundish elements, such as

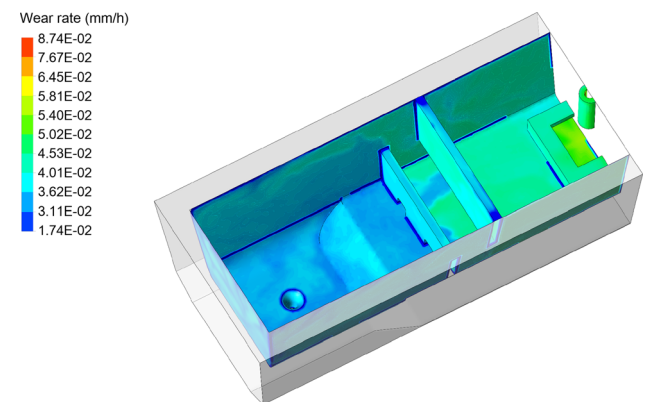


Fig. 12—Distribution of the wear rate caused by the total pressure on the entire internal refractory wall at 500 s.



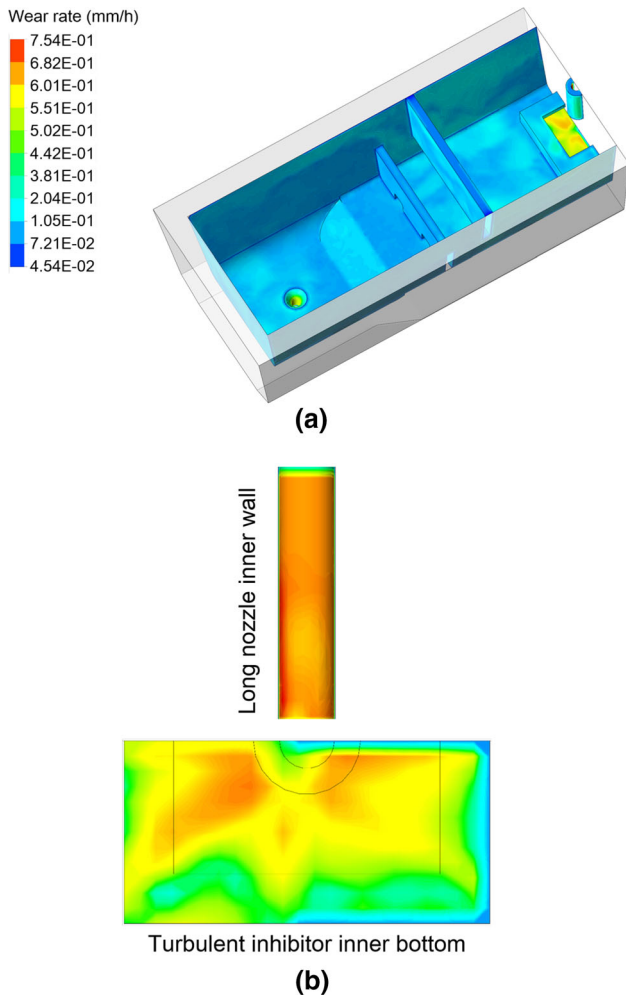


Fig. 13—Distribution of the overall wear rate caused by the wall shear stress and total pressure along the entire internal refractory wall (a) and a close-up of the long nozzle inner wall and turbulent inhibitor inner bottom (b) at 500 s.

turbulent inhibitor, weir, and dam, were negligibly small. Furthermore, the outer and inner diameters of the long nozzle are, respectively, 205 and 105 mm, which are much larger than the displacement. The influence of the long nozzle displacement on the molten steel flow was therefore neglected.

### C. Inclusion Formation and Movement

Figure 16 shows the inclusion formation and distribution inside the long nozzle and turbulent inhibitor. It can be seen that inclusions are first generated at the long nozzle inner wall as a result of serious wear. Due to high-intensity turbulence, these inclusions would be immediately taken away from the molten steel refractory and flow downward along with the molten steel. Moreover, the initial diameter of inclusions formed at the long nozzle inner wall ranged from 20 to 48  $\mu\text{m}$ . Once the molten steel impacts the turbulent inhibitor inner bottom, more inclusions would then be created. Their initial diameter (ranging from 13 to 35  $\mu\text{m}$ ) was smaller than that generated at the long nozzle inner wall.

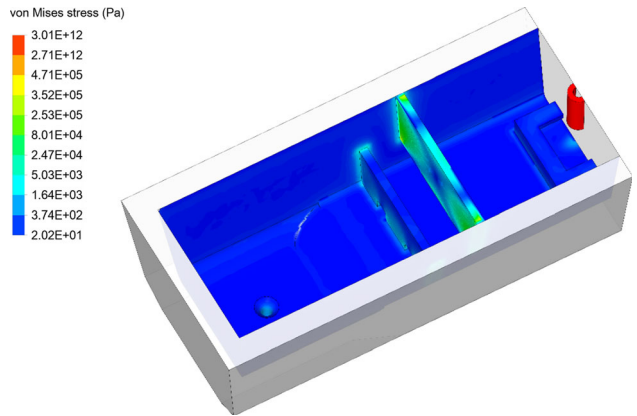


Fig. 14—Distribution of the von Mises stress along the entire internal refractory wall at 500 s.

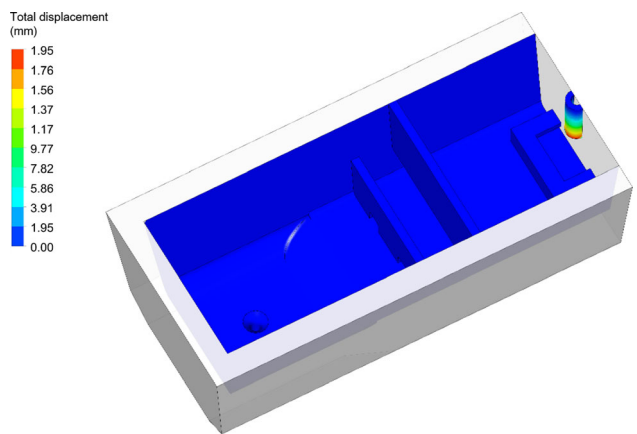


Fig. 15—Distribution of the total refractory displacement at 500 s.

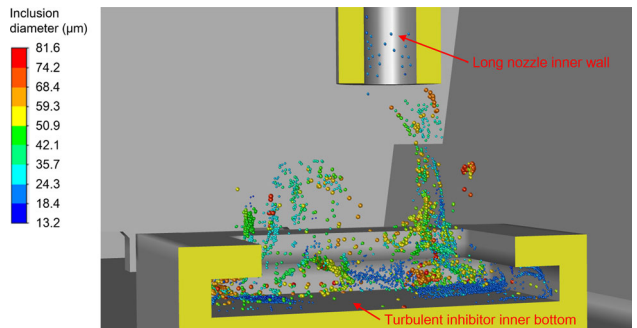


Fig. 16—Inclusion formation and distribution in the long nozzle and turbulent inhibitor.

With the collision and aggregation, the inclusions would grow, reaching a maximum diameter of 81.6  $\mu\text{m}$ . The molten steel carrying the inclusions then would go up due to the restriction of the turbulent inhibitor.

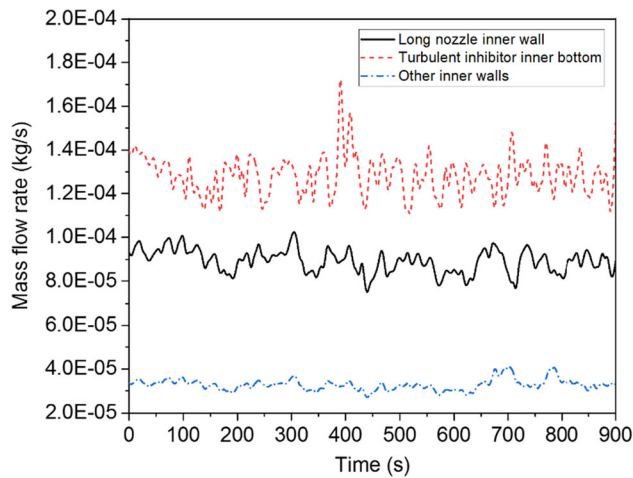


Fig. 17—Evolution of mass flow rates of the newly formed inclusions at the long nozzle inner wall, turbulent inhibitor inner bottom, and other inner walls of the tundish.

The evolution of mass flow rate of newly formed inclusions at the long nozzle inner wall, turbulent inhibitor inner bottom, and other inner walls are depicted in Figure 17. The mass flow rate fluctuates over time due to the turbulent flow pattern. The mean value of the fluctuant mass flow rate of the new inclusion generated at the turbulent inhibitor inner bottom is larger than that generated at the long nozzle inner wall. The new inclusions created at other inner walls are the slowest, since the overall wear rates at the turbulent inhibitor inner bottom and long nozzle inner wall are greater, as mentioned above. The area of the turbulent inhibitor inner bottom is larger than that of the long nozzle inner wall. Furthermore, the fluctuation amplitude of the mass flow rate of the new inclusion generated at the turbulent inhibitor inner bottom is larger than that generated at the long nozzle inner wall. It is mainly because that the flow inside the long nozzle is steadier than the impacting flow inside the turbulent inhibitor since the restriction of the solid pipe. The fluctuations of the total pressure and wall shear stress at the turbulent inhibitor inner bottom are thus greater than that at the long nozzle inner wall.

Figure 18 represents the evolution of the mass flow rate of inclusions trapped at the two free surfaces of the molten steel. It can be seen that the mass flow rate of the inclusion trapped at the first free surface rapidly rises for about 100 seconds, while that trapped at the second free surface starts to grow at about 350 seconds. The mass flow rate of the inclusion trapped at the second free surface is lower than that trapped at the first free surface, which indicates that most inclusions float upward inside the first chamber and are trapped by the first free surface. It can be concluded that the weir and dam arrangement significantly influences the inclusion removal process because their position controls the first chamber volume and the flow features within the first chamber.

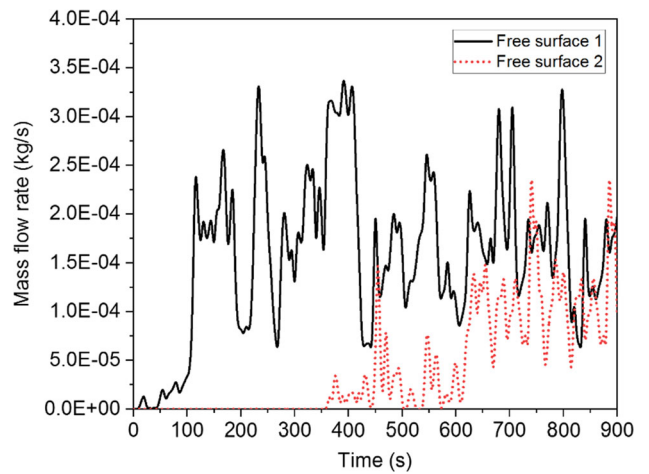


Fig. 18—Evolution of mass flow rates of the trapped inclusions at the two free surfaces of the molten steel.

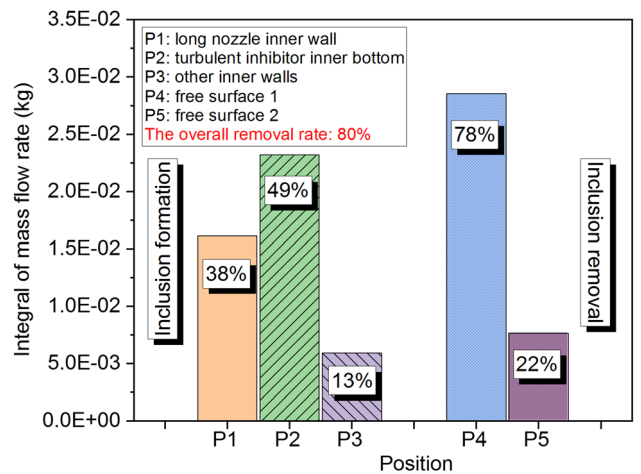


Fig. 19—Mass distribution of newly generated and trapped inclusions.

Masses of new inclusions formed at each inner wall and trapped inclusions at the two free surfaces can be obtained by integrating the inclusion mass flow rate by the flow time, as shown in Figure 19. The result indicates that 49 and 38 pct of new inclusions are created at the turbulent inhibitor inner bottom and long nozzle inner wall, respectively. In contrast, only 13 pct of new inclusions are produced at all other inner walls. During the molten steel motion, about 80 pct of the newly generated inclusions are then trapped by free surfaces (*i.e.*, the slag/steel interface), 78 pct of which are removed at the first free surface.

Since the casting speed would dramatically change the flow pattern in the tundish, the casting speed effect was also investigated using the developed numerical model, which results are demonstrated in Figure 20. The newly generated inclusion mass grew from 0.042 to 0.051 kg, with the casting speed ranging from 1.0 to 1.4 m/min, which result was quite expected. However, the mass of the removed inclusion exhibited a different pattern from the generated one. The molten steel free surface (*i.e.*,

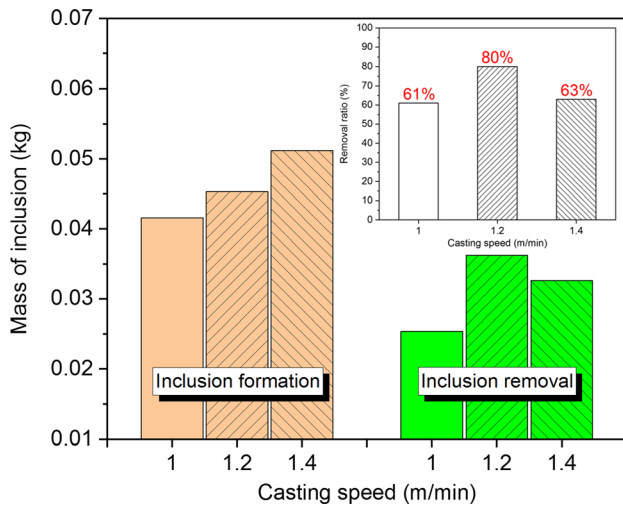


Fig. 20—Effect of casting speed on the formation and removal of inclusion in the tundish.

slag/steel interface) would trap more inclusions with the casting speed increased from 1.0 to 1.2 m/min. Simultaneously, a negative effect was produced on the inclusion removal if the casting speed continuously increased to 1.4 m/min. The removal ratio of newly generated inclusions in the tundish first grew from 61 to 80 pct, with the casting speed variation from 1.0 to 1.2 m/min and then dropped to 63 pct if the casting speed rose to 1.4 m/min. Because the increased casting speed promotes the flow-induced erosion on the refractory lining, resulting in a greater generating rate of inclusion. With a lower casting speed (1.0 m/min), the motion of the molten steel in the tundish is too slow for the removal of the inclusion. The floatation of the inclusion toward the molten slag layer is determined by its own small buoyancy. A higher casting speed (1.2 m/min) could encourage the molten steel flow as well as the inclusion motion. As a result, more inclusions would float upwards under the action of the more vigorous molten steel flow. The increasing of the inclusion removal ratio, however, would lag behind that of the inclusion generation rate when the casting speed increases to 1.4 m/min. The final removal ratio therefore reduces with the 1.4 m/min casting speed. An optimal casting speed that simultaneously ensures higher productivity and a greater inclusion removal rate can be therefore obtained for the continuous casting process.

As discussed above, the generation, motion, and removal of the exogenous inclusion could be described by the established numerical model. The results obtained strongly indicate that the exogenous inclusion tends to be produced at the turbulent inhibitor inner bottom and long nozzle inner wall due to serious wear, impacting, and washing effects. The proposed numerical model can be employed to optimize the refractory lining material and tundish elements for reducing the formation and promoting the removal of exogenous inclusions. Furthermore, the computational framework

could be extended to the simulation of other metallurgical vessels such as basic oxygen furnace, ladle, and Ruhrstahl-Heraeus degasser. The casting speed could also be carefully adjusted using the proposed numerical model for a higher productivity and inclusion removal ratio.

## V. CONCLUSIONS

To explore the formation and removal of exogenous inclusions in a full-size two-strand tundish, an unsteady 3D comprehensive numerical model of the flow pattern, temperature, and stress distribution was elaborated. The main findings can be drawn as follows:

1. The temperature drop of about 16 K (16 °C) was estimated for the molten steel moving through the tundish, and the average temperature of the refractory outer surface was assessed at about 480 K (207 °C), which agreed well with the actual tundish measurements.
2. Both the impacting and washing effects of the molten steel would damage the refractory lining. The wear rate induced by the impacting effect is smaller by one order of magnitude than that arising from the washing effect. The most damaged areas are the long nozzle inner wall and turbulent inhibitor inner bottom.
3. Higher von Mises stresses were observed at the long nozzle wall, turbulent inhibitor inner bottom, weir wall, and dam wall. The maximal value of the total displacement of 1.95 mm was observed at the lower part of the long nozzle. The total displacements of other tundish elements, such as turbulent inhibitor, weir, and dam, were negligibly small.
4. With a 1.2 m/min casting speed, 49 and 38 pct of the exogenous inclusions were created at the turbulent inhibitor inner bottom and long nozzle inner wall, respectively. In contrast, only 13 pct of new inclusions were produced at all other inner walls of the tundish. About 80 pct of the newly generated inclusions were then trapped by free surfaces (78 pct at the first free surface). Besides, the initial diameter of exogenous inclusions ranged from 13 to 48  $\mu\text{m}$ .
5. The removal ratio of the exogenous inclusion in the tundish first increased from 61 to 80 pct, with the casting speed rise from 1.0 to 1.2 m/min and then dropped to 63 pct if the casting speed grew to 1.4 m/min.

## ACKNOWLEDGMENTS

The authors' gratitude goes to the National Natural Science Foundation of China [Grant No. U1860205]. Thanks are also given to Baoshan Iron & Steel Co., Ltd. for supporting plant data.



## REFERENCES

1. K. Badr, M. Tomas, M. Kirschen, and G. McIlveney: *RHI Bull.*, 2011, vol. 1, pp. 43–50.
2. H.T. Ling, L.F. Zhang, and H. Li: *Metall. Mater. Trans. B*, 2016, vol. 47B, pp. 2991–3012.
3. M.A.S. Pour and S. Hassanpour: *Metall. Mater. Trans. B*, 2020, vol. 51B (3), p. 2199.
4. K. Badr, M. Tomas, M. Kirschen, and G. McIlveney: *Refractories Worldforum*, 2011, vol. 3 (4), pp. 111–17.
5. C.Y. Chen, Z.H. Jiang, Y. Li, M. Sun, Q. Wang, K. Chen, and H.B. Li: *ISIJ Int.*, 2020, vol. 60 (4), pp. 617–27.
6. P. Ahmadian and M. Taghizadeh: *Metall. Mater. Eng.*, 2020, vol. 26 (1), pp. 43–55.
7. Q.F. Shu, V.V. Visuri, T. Alatarvas, and T. Fabritius: *Metall. Mater. Trans. B*, 2020, <https://doi.org/10.1007/s11663-020-01955-0>.
8. Q. Wang, Y. Liu, A. Huang, W. Yan, H.Z. Gu, and G.Q. Li: *Metall. Mater. Trans. B*, 2020, vol. 51B (1), pp. 276–92.
9. C. Chen, L.T.I. Jonsson, A. Tilliander, G.G. Cheng, and P.G. Jönsson: *Metall. Mater. Trans. B*, 2015, vol. 46B (1), pp. 169–90.
10. M.Y. Zhu, W.T. Lou, and W.L. Wang: *Acta Metall. Sin.*, 2018, vol. 54 (2), pp. 131–50 (in Chinese).
11. F.G. Tan, Z. He, S.L. Jin, L.P. Pan, Y.W. Li, and B.K. Li: *Steel Res. Int.*, 2020, vol. 91, p. 1900606.
12. Z.Y. Deng, M.Y. Zhu, and S.C. Du: *Metall. Mater. Trans. B*, 2016, vol. 47B (5), pp. 3158–67.
13. A. Huang, H.Z. Gu, M.J. Zhang, N. Wang, T. Wang, and Y. Zou: *Metall. Mater. Trans. B*, 2013, vol. 44B (3), pp. 744–9.
14. M.R.M. Yazdi, A.R.F. Khorasani, and S. Talebi: *Can. Metall. Q.*, 2019, vol. 58 (4), pp. 379–88.
15. H.T. Ling, R. Xu, H.J. Wang, L.Z. Chang, and S.T. Qiu: *ISIJ Int.*, 2020, vol. 60 (3), pp. 499–508.
16. S. Chang, W.X. Huang, Z.S. Zou, B.K. Li, and R.I.L. Guthrie: *Powder Technol.*, 2020, vol. 367, pp. 396–304.
17. A. Cwudziński, J. Jowska, B. Gajda, and A. Hutny: *Ironmak. Steelmak.*, 2020, <https://doi.org/10.1080/03019233.2019.1708670>.
18. P.H.R. Vaz de Melo, J.J.M. Peixoto, G.S. Galante, B.H.M. Loiola, C.A. da Silva, I.A. da Silva, and V. Seshadri: *J. Mater. Res. Technol.*, 2019, vol. 8 (5), pp. 3764–71.
19. V. Singh, A.R. Pal, and P. Panigrahi: *ISIJ Int.*, 2008, vol. 48 (4), pp. 430–37.
20. K. Chattopadhyay, M. Isac, and R.I.L. Guthrie: *ISIJ Int.*, 2010, vol. 50 (3), pp. 331–48.
21. S. Riaz, K.C. Mills, and K. Bain: *Ironmak. Steelmak.*, 2002, vol. 29 (2), pp. 107–13.
22. T. Momma and A. Lichtarowicz: *Wear*, 1995, vols. 186–187, pp. 425–36.
23. P. Kumar, N. Kumar, and H. Kumar: *Int. J. Mech. Mechatron. Eng.*, 2017, vol. 11 (2), pp. 299–302.
24. M.C. Mantovani, L.R. Moraes, Jr, R. Leandro da Silva, E.F. Cabral, E.A. Possente, C.A. Barbosa, and B.P. Ramos: *Ironmak. Steelmak.*, 2013, vol. 40 (5), pp. 319–25.
25. S. Schachner, S.L. Jin, D. Gruber, and H. Harmuth: *Ceram. Int.*, 2019, vol. 45, pp. 9483–90.
26. E. Gutiérrez, S. Garcia-Hernandez, and J. de Jesús Barreto: *Steel Res. Int.*, 2019, 1900328.
27. M. Warzecha, T. Merder, P. Warzecha, and Stradomski: *ISIJ Int.*, 2013, vol. 53(11), pp. 1983–92.
28. U.D. Salgado, C. Weiß, S.K. Michelic, and C. Bernhard: *Metall. Mater. Trans. B*, 2018, vol. 49B, pp. 1632–43.
29. C.J. Xuan, E.S. Persson, R. Sevastopolev, and M. Nzotta: *Metall. Mater. Trans. B*, 2019, vol. 50B, pp. 1957–73.
30. Q. Wang, Y. Liu, A. Huang, W. Yan, H.Z. Gu, and G.Q. Li: *Powder Technol.*, 2020, vol. 367, pp. 358–75.
31. L.F. Zhang, S. Taniguchi, and K.K. Cai: *Metall. Mater. Trans. B*, 2000, vol. 31B, pp. 253–66.
32. H. Harmuth and G.M. Xia: *ISIJ Int.*, 2015, vol. 55 (4), pp. 775–80.
33. N. Kasai and M. Iguchi: *ISIJ Int.*, 2007, vol. 47 (7), pp. 982–87.
34. Y.L. Zhang, B.S. McLaury, and S.A. Shirazi: *J. Fluids Eng.*, 2009, vol. 131(3), 031303.
35. Z.Q. Liu, A. Vakhrushev, M. Wu, A. Kharicha, A. Ludwig, and B.K. Li: *Metall. Mater. Trans. B*, 2019, vol. 50B, pp. 543–54.
36. K. Jin, S.P. Vanka, and B.G. Thomas: *Metall. Mater. Trans. B*, 2018, vol. 49B, pp. 1360–77.
37. S. Kawai and J. Larsson: *Phys. Fluids*, 2012, vol. 24, p. 015105.
38. Z.Q. Liu, Y.D. Wu, and B.K. Li: *Powder Technol.*, 2020, vol. 374, pp. 470–81.
39. A. López, M.T. Stickland, and W.M. Dempster: *Comput. Phys. Commun.*, 2018, vol. 227, pp. 27–41.
40. G.V. Messa and S. Malavasi: *Wear*, 2018, vols. 398–399, pp. 127–45.
41. M.H. Wang, C. Huang, K. Nandakumar, P. Minev, J. Luo, and S. Chiovelli: *Int. J. Comput. Fluid D.*, 2009, vol. 23(2), pp. 155–72.
42. J. Zhang, F. Darihaki, and S.A. Shirazi: *Wear*, 2019, vols. 430–431, pp. 191–201.
43. T. Nazari, A. Rabiee, and H. Kazeminejad: *Nucl. Eng. Technol.*, 2019, vol. 51, pp. 573–8.
44. M.R. Motley, Z. Liu, and Y.L. Young: *Compos. Struct.*, 2009, vol. 90, pp. 304–13.
45. D.S. Xie, C. Garlick, and T. Tran: *ISIJ Int.*, 2005, vol. 45 (2), pp. 175–82.
46. R.C. Das, S. Fouzdar, U.K. Chatterjee, and A.R. Pal: *Trans. Ind. Ceram. Soc.*, 2007, vol. 66 (4), pp. 193–202.
47. N.N. Tripathi, M. Nzotta, A. Sandberg, and S.C. Du: *Ironmak. Steelmak.*, 2004, vol. 31 (3), pp. 235–40.
48. M.J. Zhang, X.L. Lin, Y. Wu, and A. Huang: *Adv. Mater. Res.*, 2010, vols. 105–106, pp. 142–45.
49. P.K. Iwamasa, G.A. Caffery, W.D. Warnica, and S.R. Alias, Modelling of iron flow, heat transfer, and refractory wear in the hearth of an iron blast furnace, International Conference on CFD in Mineral & Metal Processing and Powder Generation, CSIRO, 1997, pp. 285–96.
50. H.J. Zhu, Q. Pan, W.L. Zhang, G. Feng, and X. Li: *Nucl. Eng. Des.*, 2014, vol. 273, pp. 396–411.
51. Z.S. Li, K. Mukai, and Z.N. Tao: *ISIJ Int.*, 2000, vol. 40 (S1), pp. S101–S105.
52. A.P. Luz, F.C. Leite, M.A.M. Brito, and V.C. Pandolfelli: *Ceram. Int.*, 2013, vol. 39, pp. 7507–15.
53. H.B. Yin, H. Shibata, T. Emi, and M. Suzuki: *ISIJ Int.*, 1997, vol. 37 (10), pp. 936–45.
54. H.B. Yin, H. Shibata, T. Emi, and M. Suzuki: *ISIJ Int.*, 1997, vol. 37 (10), pp. 946–55.
55. H. Barati, M. Wu, A. Kharicha, and A. Ludwig: *Powder Technol.*, 2018, vol. 329, pp. 181–98.
56. W. Ludwig and P. Pluszka: *Powder Technol.*, 2018, vol. 328, pp. 375–88.
57. Y. Miki and B.G. Thomas: *Metall. Mater. Trans. B*, 1999, vol. 30B, pp. 639–54.
58. M. Vanderroost, F. Ronsse, K. Dewettinck, and J.G. Pieters: *Powder Technol.*, 2012, vol. 221, pp. 155–63.
59. J. Zhang, J.C. Mi, and H. Wang: *Aerosol Sci. Technol.*, 2012, vol. 46, pp. 622–30.
60. H. Lei, Y. Zhao, and D.Q. Geng: *ISIJ Int.*, 2014, vol. 54 (7), pp. 1629–37.
61. L.M. Li, B.K. Li, and Z.Q. Liu: *ISIJ Int.*, 2017, vol. 57 (11), pp. 1980–89.
62. S. Joo, J.W. Han, and R.I.L. Guthrie: *Metall. Trans. B*, 1993, vol. 24B, pp. 767–77.
63. Z.W. Hu, Y. Ci, and Z. Xie: *ISIJ Int.*, 2011, vol. 51 (10), pp. 1674–81.
64. L.F. Zhang: *Steel Res. Int.*, 2005, vol. 76 (11), pp. 784–96.
65. Q. Wang, B.K. Li, and F. Tsukihashi: *ISIJ Int.*, 2014, vol. 54 (2), pp. 311–20.
66. J.H. Shin, Y. Chung, and J.H. Park: *Metall. Mater. Trans. B*, 2017, vol. 48B, pp. 46–59.
67. P.Y. Ni, L.T.I. Jonsson, M. Ersson, and P.G. Jönsson: *Steel Res. Int.*, 2017, vol. 83(3), 1600155.
68. D. Kumar, K.C. Ahlborg, and P.C. Pistorius: *Metall. Mater. Trans. B*, 2019, vol. 50B, pp. 2163–74.
69. M.A. van Ende, M.X. Guo, E. Zingrebe, B. Blanpain, and I.H. Jung: *ISIJ Int.*, 2013, vol. 53 (11), pp. 1974–82.
70. W.Z. Wu, N. Dogan, and K.S. Coley: *Metall. Mater. Trans. B*, 2017, vol. 48B, pp. 2092–2103.

71. Y. Yang, H. Nomura, and M. Takita: *Int. J. Cast Metals Res.*, 1996, vol. 9, pp. 27–35.
72. N. Almohammed and M. Breuer: *Int. J. Multiph. Flow*, 2016, vol. 85, pp. 142–56.
73. J.C.R. Hunt, A.A. Wray, and P. Moin, Eddies, stream and convergence zones in turbulent flows, Proceedings of the Summer Program, Center for Turbulence Research, 1988, pp. 193–208.
74. W.S. Fu, Y.C. Lai, and C.G. Li: *Int. Commun. Heat Mass Transf.*, 2013, vol. 45, pp. 41–6.
75. J.M. Zhan, Y.T. Li, W.H. Onyx Wai, and W.Q. Hu: *Phys. Fluids*, 2019, vol. 31, 121701.

**Publisher's Note** Springer Nature remains neutral with regard to jurisdictional claims in published maps and institutional affiliations.